Pseudopotential Calculation of the Optical Constants of MgO from 7–28 eV

C. Y. Fong* and W. Saslow*
Department of Physics, University of California, Berkeley, California

AND

Marvin L. Cohen†
Department of Physics and Inorganic Materials Research Division, Lawrence Radiation Laboratory, University of California, Berkeley, California

(Received 17 August 1967)

The electronic band structure of MgO is computed using the empirical pseudopotential method. The resulting energy bands are then used to calculate the optical constants over a wide range in energy. The optical constants calculated are the real and imaginary parts of the dielectric function, the reflectivity, and the imaginary part of the inverse dielectric function. Optical interband transitions are identified, and a comparison between experiment and theory is made.

INTRODUCTION

NEW measurements by Roessler and Walker[1] (RW) of the optical constants of MgO over a wide energy range (5–28 eV) have motivated us to extend and refine a previous calculation[2] of the electronic band structure of this material using the empirical pseudopotential method (EPM). This energy-band calculation enabled us to determine the real and imaginary parts of the dielectric function $\epsilon_1(\omega)$ and $\epsilon_2(\omega)$, the reflectivity $R(\omega)$, and the imaginary part of the inverse dielectric function $\mathrm{Im}[1/\epsilon(\omega)]$, over an energy range from the fundamental gap energy to the plasma energy.

In Ref. 2 (I) it was only possible to compare the theoretical ϵ_2 with the experimental reflectivity as an experimental ϵ_2 was not available. In addition, previous measurements[2] were made only up to 14.5 eV and the comparison between experiment and theory was therefore limited to this range. Except for small energy shifts, the present calculation gives essentially the same results as I for energies below 14.5 eV. For energies from 14.5–28 eV, the availability of experimental data allows a direct comparison between theory and experiment over the entire energy range, and hence a thorough test of the theory over a wide energy range can be made. This is the first such comparison between theory and experiment to be reported.

A critical point (cp) analysis is made to identify the optical structure in terms of interband transitions. The structure and symmetries of the cp's are determined through the use of the energy band contours given in Figs. 4–6 and 9–14. The contributions of two important interband transitions are evaluated, and these contributions are given in Figs. 7 and 8.

It is found in comparing the theoretical calculations and the experimental measurements of the optical constants [in particular $\epsilon_2(\omega)$] that there is good agreement between theory and experiment. This is particularly impressive when one considers that the EPM assumes a pseudopotential which is independent of energy and wave vector.

CALCULATIONS

The band-structure calculation presented here employs the empirical pseudopotential method.[3] This method involves adjusting pseudopotential form factors to give a few of the principal optical transitions (e.g., the fundamental gap). These form factors are then used to determine the electronic energy bands over a wide range in energy and at many points in the Brillouin zone. Because this method is described elsewhere[2,3] and the application to the case of MgO is given in I, we will just give a few of the important expressions to define the form factors and then go directly to a discussion of the form factors and the band structure.

The pseudopotential Hamiltonian has the form

$$H=-(\hbar^2/2m)\nabla^2+V(\mathbf{r}). \tag{1}$$

The weak pseudopotential $V(\mathbf{r})$ is expanded in the reciprocal lattice

$$V(\mathbf{r})=\sum_{|\mathbf{G}|} V(\mathbf{G})e^{i\mathbf{G}\cdot\mathbf{r}}, \tag{2}$$

Table I. A comparison of MgO form factors (in Ry) used in the present work with those used in Ref. 2.

Form factor	Current calculation (Ry)	Ref. 2 (I) (Ry)
$V^S(200)$	−0.0956	−0.1008
$V^S(220)$	0.0705	0.0745
$V^S(222)$	0.0191	0.0238
$V^A(111)$	0.2471	0.2500
$V^A(311)$	0.0136	0.0160

* Supported by the National Science Foundation.
† Alfred P. Sloan Fellow.
[1] D. M. Roessler and W. C. Walker, Phys. Rev. **159**, 733 (1967) (hereafter referred to as RW).
[2] M. L. Cohen, P. J. Lin, D. M. Roessler, and W. C. Walker, Phys. Rev. **155**, 992 (1967) (hereafter referred to as I).
[3] M. L. Cohen and T. K. Bergstresser, Phys. Rev. **141**, 789 (1966), and references therein.

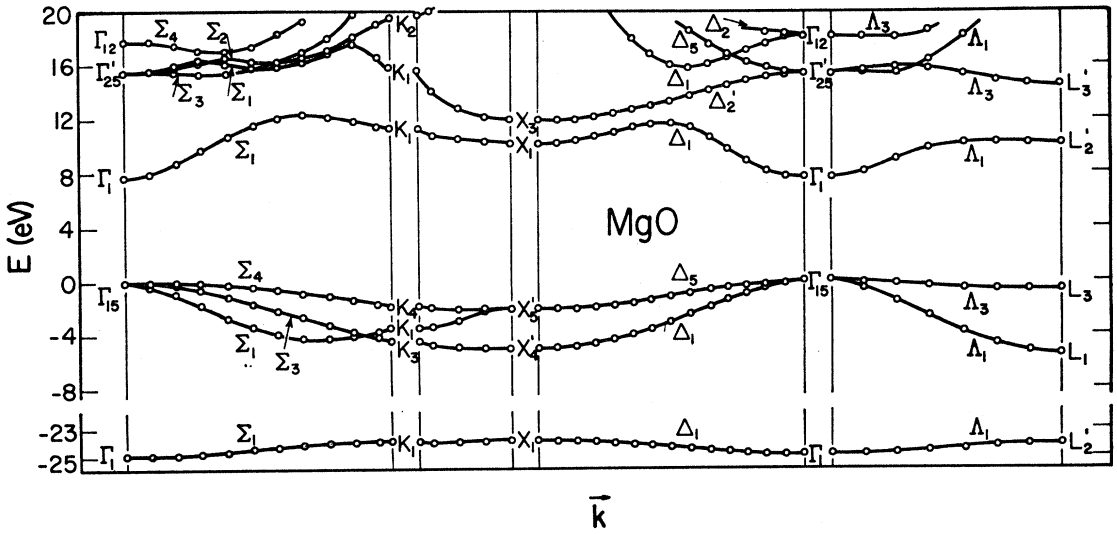

FIG. 1. Electronic energy-band structure of MgO.

where **G** is a reciprocal lattice vector, and

$$V(\mathbf{G})=\sum_{\alpha} V_{\alpha}(\mathbf{G})S_{\alpha}(\mathbf{G}), \tag{3}$$

$$S_{\alpha}(G)=e^{i\mathbf{G}\cdot\tau\alpha}, \tag{4}$$

$$V_{\alpha}(G)=\frac{2}{\Omega}\int V_{\alpha}(r)e^{-i\mathbf{G}\cdot\mathbf{r}}d^{3}\mathbf{r}, \tag{5}$$

where $V_{\alpha}(\mathbf{r})$ is an atomic pseudopotential, τ_{α} is the position vector of an atom, Ω is the unit cell volume, and α is the index of the atom in a unit cell.

Magnesium oxide has the rocksalt structure with a lattice constant of $a=4.21$ Å. If the origin of the coordinate system is taken at a Mg site, the vectors $\tau_1=(0,0,0)$ and $\tau_2=(\frac{1}{2},\frac{1}{2},\frac{1}{2})$ give the positions of the Mg and O atoms in the cell. The form factors can then be divided[2,3] into symmetric and antisymmetric components given by

$$V(\mathbf{G})=V_1(\mathbf{G})+V_2(\mathbf{G})=2V_G{}^S, \quad \text{for } |G|^2 \text{ even} \tag{6}$$

$$V(\mathbf{G})=V_1(\mathbf{G})-V_2(\mathbf{G})=2V_G{}^A, \quad \text{for } |G|^2 \text{ odd} \tag{7}$$

where the subscripts 1 and 2 refer to the two atoms in the unit cell.

A comparison of the form factors used in the present calculation and in I is given in Table I. The differences are small, the largest difference being approximately 0.005 Ry. The changes in the form factors were made to improve the agreement between the low-energy gaps of

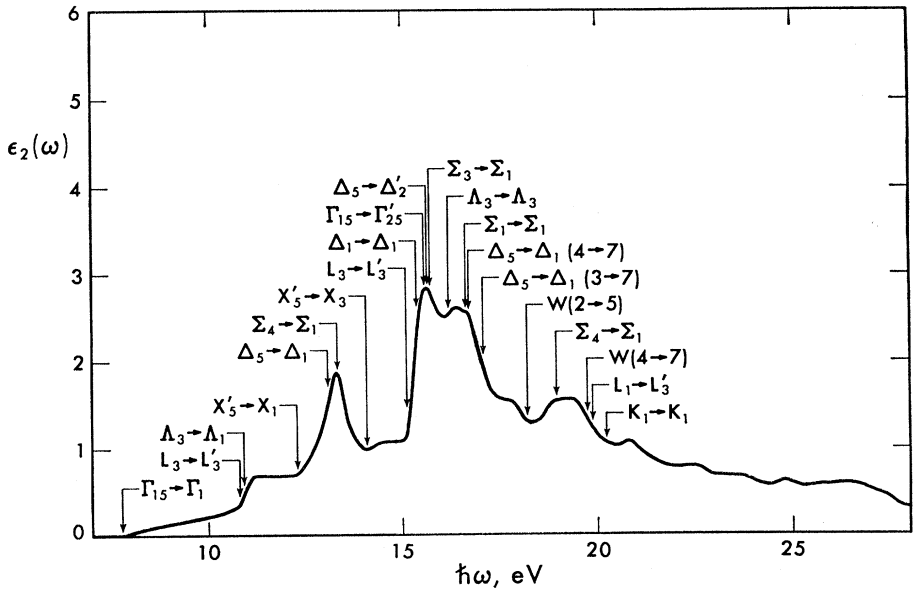

FIG. 2. Theoretical $\epsilon_2(\omega)$ with constant matrix elements.

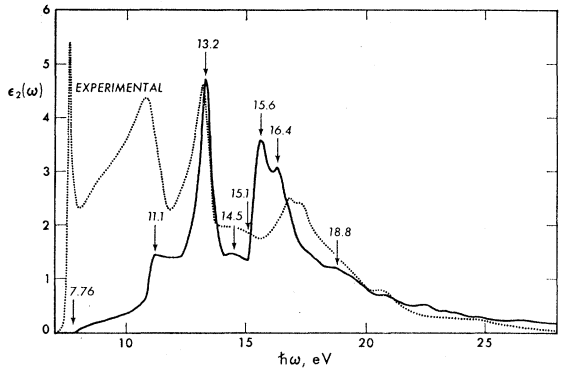

FIG. 3. Theoretical $\epsilon_2(\omega)$ with matrix elements computed using pseudo-wave-functions.

the band-structure calculation and the recent RW values obtained from the experimental ϵ_2.

The determination of ϵ_2 requires a knowledge of the energy bands throughout the Brillouin zone[4] since this function has the form

$$\epsilon_2(\omega)=\frac{e^2h^2}{m}\sum_{ij}\frac{2}{(2\pi)^3}\int\frac{f_{ij}(k)dS}{E_{ij}|\nabla_k E_{ij}|}, \tag{8}$$

where

$$f_{ij}(k)=\frac{2}{3m}\frac{|\langle k,i|\mathbf{P}|k,j\rangle|^2}{E_{ij}} \tag{9}$$

is the interband oscillator strength and S is a surface of constant interband energy $E_{ij}=E_j-E_i$. The prominent optical structure in $\epsilon_2(\omega)$ originates from Van Hove[5,6] singularities at the critical points, where $\nabla_k E_{ij}=0$. These critical points can be classified[4] according to symmetry (minima, saddle points, and maxima) M_0, M_1, M_2, and M_3.

The numerical calculations of Eqs. (8) and (9) are done in the same manner as in I. After $\epsilon_2(\omega)$ is determined, $\epsilon_1(\omega)$ is evaluated by a Kramers-Kronig analysis. The functions $\epsilon_1(\omega)$ and $\epsilon_2(\omega)$ are then used to obtain the reflectivity $R(\omega)$ and $\mathrm{Im}[1/\epsilon(\omega)]$.

TABLE II. Identification of prominent optical structure and comparison of the energies (in eV) between the calculated and measured ϵ_2.

Prominent interband transitions	Energy (theory) (eV)	Energy (expt) (eV)
$\Gamma_{15}\rightarrow\Gamma_1$	7.76	7.77
$\Lambda_3\rightarrow\Lambda_1$ (10.8)	11.1 (peak)	10.8 (peak)
$L_3\rightarrow L_{2'}$		
$\Delta_5\rightarrow\Delta_1$	13.2 (peak)	13.2 (peak)
$\Sigma_4\rightarrow\Sigma_1$ (13.3) (4 → 5)		
$L_3\rightarrow L_{3'}$	15.2	15.7
$\Sigma_3\rightarrow\Sigma_1$	15.7 (peak)	16.8 (peak)
$\Lambda_3\rightarrow\Lambda_3$	16.2 (peak)	17.4 (peak)
$\Sigma_4\rightarrow\Sigma_1$ (4 → 6)	19	20.5

[4] D. Brust, Phys. Rev. **134**, A1337 (1964).
[5] L. Van Hove, Phys. Rev. **89**, 1189 (1953).
[6] J. C. Phillips, Phys. Rev. **104**, 1263 (1956).

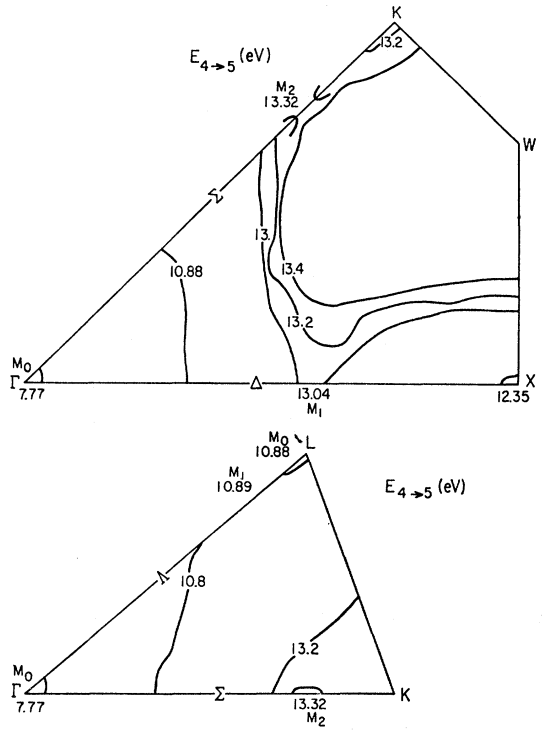

FIG. 4. Energy contours for 4 → 5 transitions in the ΓKL and ΓKWX planes.

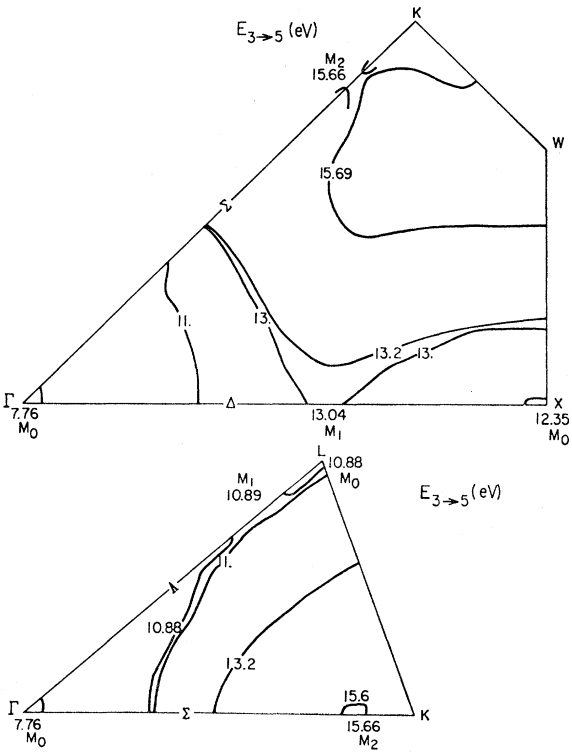

FIG. 5. Energy contours for 3 → 5 transitions in the ΓKL and ΓKWX planes.

RESULTS

The band structure of MgO is given in Fig. 1 along several symmetry lines in the Brillouin zone. The lowest band at about 25 eV below the top of the valence band is given only for completeness. It is not expected that the pseudopotential calculation determines the energy of this band accurately. Since the optical structure discussed in this work originates from transitions involving the upper valence bands and the lower conduction bands, the inaccuracy in determining the lowest valence band has no effect on the results of the $\epsilon_2(\omega)$ calculation.

The band structure is essentially the same as that given[7] in I except for small energy shifts and small changes in shape. The theoretical and experimental values for the energies of the prominent optical structure in $\epsilon_2(\omega)$ are listed in Table I. The calculated critical-point energies, the associated band transition, and the symmetry of the critical points are given in Table II. Figure 2 gives the calculated $\epsilon_2(\omega)$ assuming constant matrix elements in Eq. (9). In Fig. 3, $\epsilon_2(\omega)$ is plotted with matrix elements computed using pseudopotential wave functions as in I.

The top of the valence band and the bottom of the conduction band are both at Γ and the fundamental gap is therefore direct. The exciton associated with this gap has been studied[1,2,8,9] and the line shape was fitted by a Lorentzian curve yielding an experimental gap energy of 7.77 eV. The theoretical value for $\Gamma_{15} \rightarrow \Gamma_1$ is 7.76 eV and the cp has M_0 symmetry as is shown in the total $\epsilon_2(\omega)$, the energy contours (Figs. 4–6), and the ϵ_2's for the transitions between bands 4 and 5, and 4 and 6 (Figs. 7 and 8).

It is interesting to note that the band-structure calculation gives some fine structure in the conduction band near Γ. The conduction band in the X direction is flat near Γ and then dips about 0.07 eV at a k vector

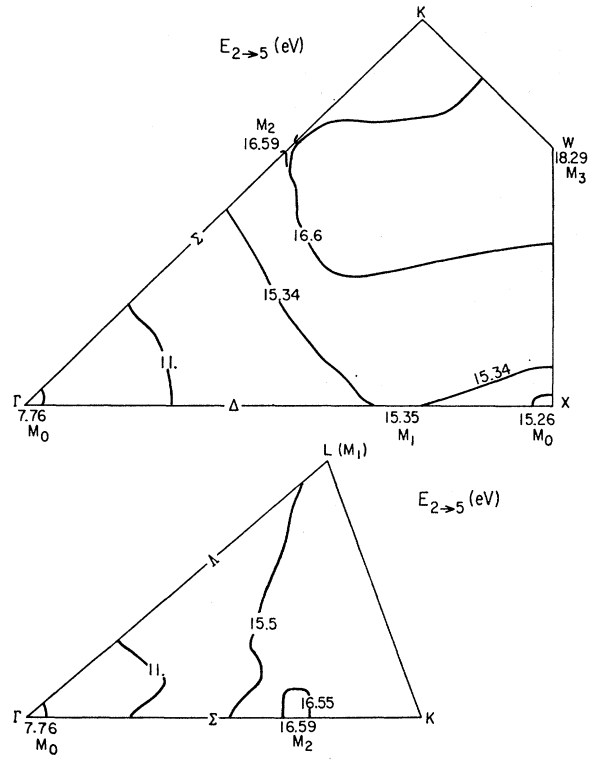

FIG. 6. Energy contours for $2 \rightarrow 5$ transitions in the ΓKL and ΓKWX planes.

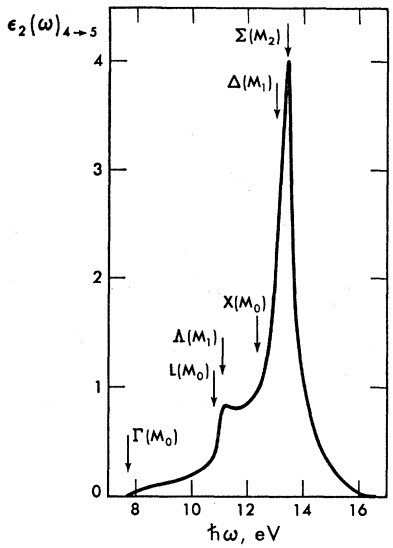

FIG. 7. Contributions to ϵ_2 from $4 \rightarrow 5$ transitions.

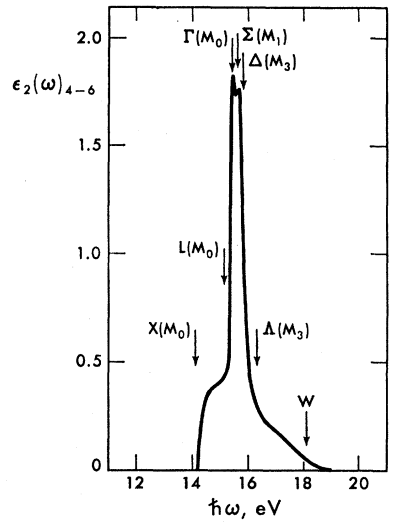

FIG. 8. Contributions to ϵ_2 from $4 \rightarrow 6$ transitions.

[7] The band Γ_{25}'-Δ_1 and Γ_{12}-Δ_2 were omitted in Ref. 2, but they are included here. The change in potential does cause some change in the shape of bands 6, 7, and 8 along Σ. The scale has been changed from I.

[8] D. M. Roessler and W. C. Walker, Phys. Rev. Letters 17, 319 (1966).

[9] These references are given in Ref. 1.

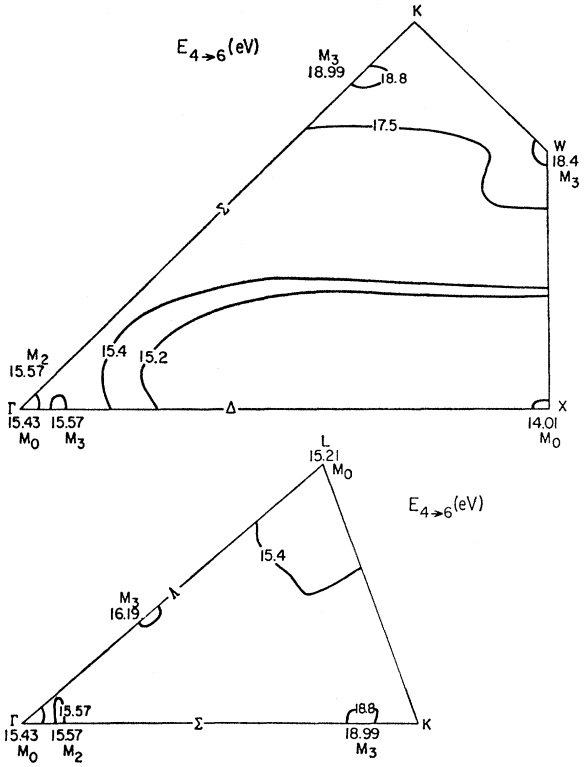

FIG. 9. Energy contours for $4 \to 6$ transitions in the ΓKL and ΓKWX planes.

which is approximately 3% of the Brillouin-zone k vector. This structure is relatively insensitive to variations in the pseudopotential. It is difficult at this time to determine whether the effects of this structure can be observed or if it is connected with the structure seen in the exciton peak.

The next structure in $\epsilon_2(\omega)$ which appears around 11 eV arises from $4 \to 5$ and $3 \to 5$ band transitions (Figs. 7 and 8). This structure is associated with $L_3 \to L_2'$ and $\Lambda_3 \to \Lambda_1$ transitions with cp symmetry M_0 and M_1. The M_0 cp lies only slightly below the M_1 cp in energy and as can be seen from the ΓKL plane energy contours of Figs. 4 and 5, a broad region of the zone near L contributes to the 11.1-eV peak. Although in this work we are primarily interested in the identification of the optical structure and in the determination of the energy of this structure and only secondarily in the peak heights, we note that the L-Λ peak is too small in the calculated $\epsilon_2(\omega)$ as calculated with constant matrix elements and with pseudo-wave-function matrix elements. It is not clear at present why this structure is too small. A plausible explanation is that the momentum matrix elements for this region are underestimated. We note that if this structure were stronger in the $\epsilon_2(\omega)$, the energy region between 7.77 and 11.0 eV would be filled in, and the theoretical $\epsilon_2(\omega)$ would look much more like the experimental curve in this region.

The peak centered around 13.2 eV is the most prominent peak in the spectrum. This structure is caused by $4 \to 5$ and $3 \to 5$ transitions along Δ and $4 \to 5$ transitions along Σ (Fig. 7). The structure begins with an M_0 cp at 12.35 eV arising from $X_5' \to X_1$ transitions (Figs. 4 and 5). The main peak is caused primarily by $4 \to 5$ transitions; in particular, an M_1 along Δ and an M_2 along Σ. This peak is usually referred to as the X peak because this structure varies in the same way as the $X_5' \to X_1$ splitting with changes in the potential. The shape of the calculated X peak (see Fig. 3) is very close to the measured structure observed by RW.

The lack of structure between about 14 and 15 eV is very interesting and it appears in both the calculated and measured $\epsilon_2(\omega)$. This region represents the separation between $4 \to 5$ and $3 \to 5$ band transitions, i.e., the top two valence bands and the bottom conduction bands, and transitions involving lower valence bands and higher conduction bands. There is one exception to this, the $4 \to 6$ transition $X_5' \to X_3$ is found to be 14.02 eV, which is at the beginning of this dip region, but this transition contributes only a weak M_0 cp (Figs. 9 and 10), and we assign it to the 14 eV region in the experimental curve.

The structure in $\epsilon_2(\omega)$ above 15 eV arises from $2 \to 5$, $3 \to 5$, $2 \to 6$, $3 \to 6$, $4 \to 6$, $3 \to 7$, and $4 \to 7$ band transitions. The energy contours for these transitions are given in Figs. 5 and 6, and 9–14. The calculated energies for the dominant transitions differ from the experiment by about 1 eV, and the experimental

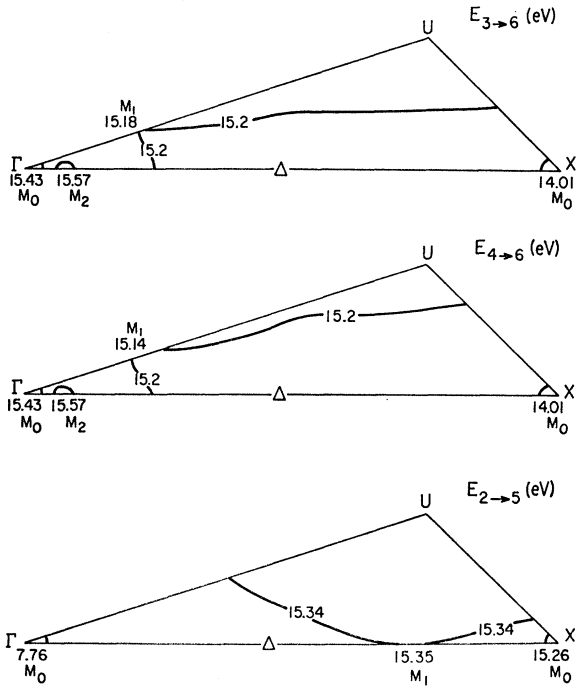

FIG. 10. Energy contours for $3 \to 6$, $4 \to 6$, and $2 \to 5$ transitions in the ΓXU plane.

structure is broader than the theoretical structure in this region. Even with these differences, we still consider this to be good agreement between theory and experiment since the energy range we care considering is 21 eV.

The measured $\epsilon_2(\omega)$ shows a twin-peaks structure in the 15.5–18-eV range with smaller structure on the low- and high-energy sides of this region. Similar structure is seen in the calculated $\epsilon_2(\omega)$ in the 15.2–17-eV region as shown in Fig. 3. There are many cp's which contribute to $\epsilon_2(\omega)$ in this region, but we will discuss only the strongest of these. It should be emphasized that the agreement between experiment and theory in this region is lost if the potential is slightly changed.

For energies just above 15 eV, the calculated $\epsilon_2(\omega)$ rises more sharply than the measured $\epsilon_2(\omega)$ in the corresponding energy region ($\sim$15.5 eV), indicating that the calculated cp's are probably closer together in energy than they should be. The beginning structure is caused by two M_0 cp's and M_1 cp. The M_0's contribute strongly since they involve transitions between doubly degenerate ($L_3 \rightarrow L_3$, 15.2-eV) and triply degenerate ($\Gamma_{15} \rightarrow \Gamma_{25}'$, 15.43-eV) bands. The M_1 cp at 15.35 eV is also strong and it arises from $\Delta_1 \rightarrow \Delta_1$ transitions (Figs. 6 and 10).

The region around 15.6 eV also involves several transitions; $4 \rightarrow 6$ transitions contribute strongly. The two main cp's involved come from $\Delta_5 \rightarrow \Delta_2'$ and $\Sigma_4 \rightarrow \Sigma_1$ transitions near Γ. In both cases, however, the region close to the cp contributes rather weakly, and the contributions come from an extended region of the zone (Figs. 9 and 10). In contrast, the cp $\Delta_5 \rightarrow \Delta_2'$ at 15.57 eV coming from $3 \rightarrow 6$ transitions contributes strongly close to the cp region and the characteristics of this cp are not smeared out by the large background. A $\Sigma_3 \rightarrow \Sigma_1$ M_2 cp at 15.66 coming from $3 \rightarrow 5$ transitions also contributes strongly in this region.

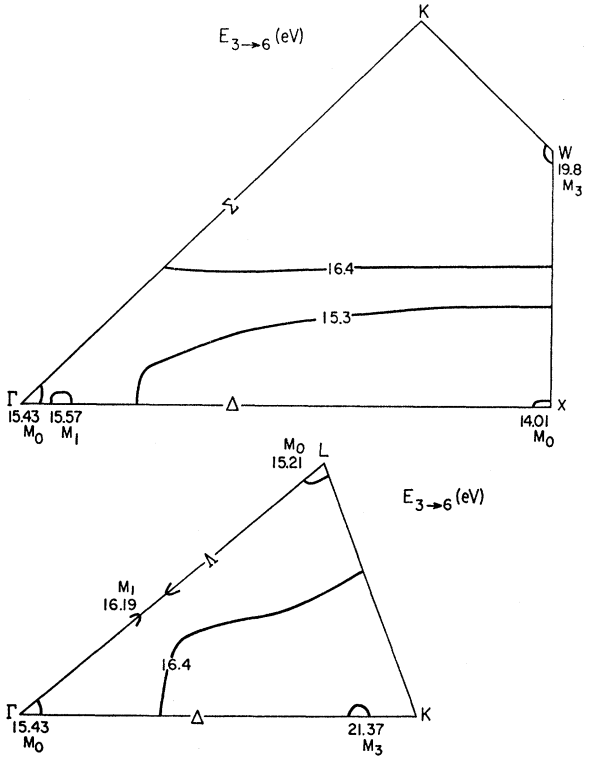

FIG. 11. Energy contours for $3 \rightarrow 6$ transitions in the ΓKL and ΓKWX planes.

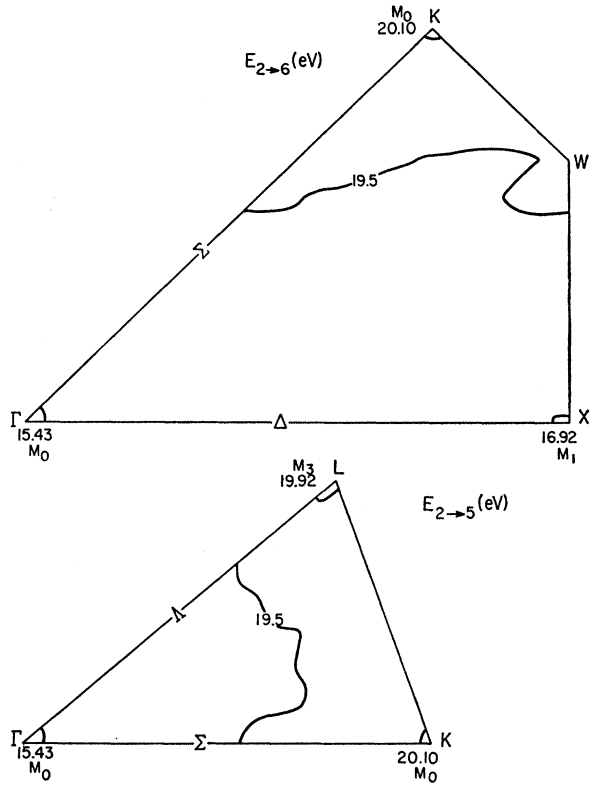

FIG. 12. Energy contours for $2 \rightarrow 6$ transitions in the ΓKL and ΓKWX planes.

The second peak of the twin-peaks structure begins with a strong peak coming from a transition between doubly degenerate bands, $\Lambda_3 \rightarrow \Lambda_3$. The cp's arising from these transitions have both M_2 and M_3 character. The strong M_3 caused by $4 \rightarrow 7$ transitions tends to flatten the peak in this region. The structure at 16.4 and 16.6 eV arises from $4 \rightarrow 7$ and $3 \rightarrow 7$ transitions. The $\Sigma_4 \rightarrow \Sigma_2$ and $\Delta_5 \rightarrow \Delta_1$ M_3 cp's contribute to the $4 \rightarrow 7$ peak and regions near Δ and Σ contribute to the $3 \rightarrow 7$ peak.

The decrease in $\epsilon_2(\omega)$ in the experimental curve in this region is less rapid than the calculated curve. Again, the cp's may lie too close together in energy. The main contributions in this region come from $X_4' \rightarrow X_3$ and $\Delta_5 \rightarrow \Delta_1$ transitions at 16.9 and 17.01 eV.

The measured $\epsilon_2(\omega)$ shows little structure for energies above 17 eV except for a bump around 20.5 eV. The $\epsilon_2(\omega)$ in the region from 18–20 eV is still fairly large, and it is possible that this structure exists which has not

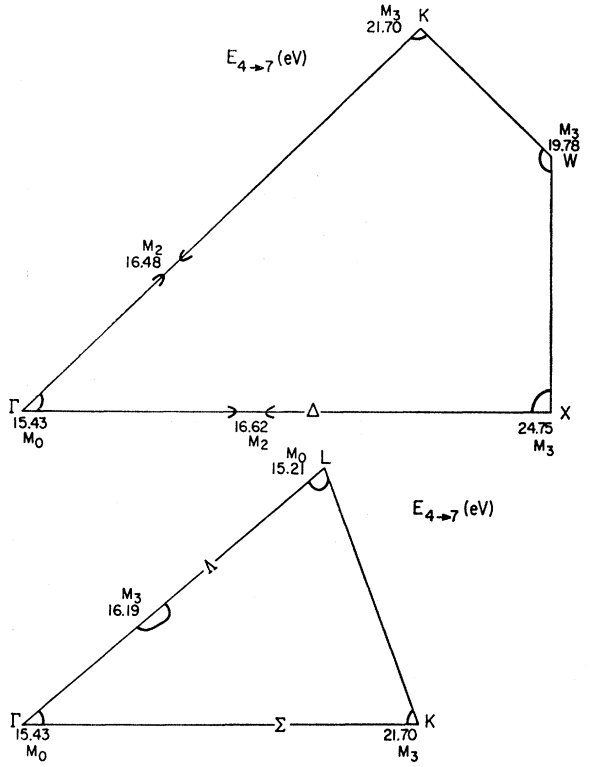

FIG. 13. Energy contours for $4 \rightarrow 7$ transitions in the ΓKL and ΓKWX planes.

been resolved. The calculated $\epsilon_2(\omega)$ with constant matrix elements does show some structure in this region. The $\epsilon_2(\omega)$ with pseudo-wave-function matrix elements has just a hint of this structure, and it resembles the measured $\epsilon_2(\omega)$. The origin of the main structure is listed in Table III. The bump in the constant matrix $\epsilon_2(\omega)$ (Fig. 2) at 19 eV comes from $4 \rightarrow 6$ Σ transitions (Fig. 9) in a region near W. The small structure around 20.5 eV in Fig. 3 comes from $4 \rightarrow 7$ transitions near K and $3 \rightarrow 7$ transitions near W. It is difficult at this time to make a detailed comparison of the calculated curve with experiment because of the lack of experimental structure. More refined measurements of the spectrum in this region would be very helpful. Such measurements would make these assignments possible.

The function $\epsilon_2(\omega)$ as given in Fig. 3 was used to obtain $\epsilon_1(\omega)$ by means of the Kramers-Kronig relation. The $\epsilon_2(\omega)$ function was multiplied by a scale factor 1.1 to convert the units before the Kramers-Kronig analysis was done. The resulting $\epsilon_1(\omega)$ appears in Fig. 15. Since the theoretical $\epsilon_2(\omega)$ does not contain the exciton peak and the $\epsilon_2(\omega)$ in the region of 8–11 eV is too flat, the ϵ_1 is not very accurate in this region. In fact, a peak occurs near the threshold. The measured dip between 11 and 12 eV is reproduced and the general shape of the rest of the curve is very similar to the curve derived from experiment. The calculated ϵ_1 goes to zero at 20 eV and

TABLE III. Calculated critical-point energies, associated band transitions, and critical-point symmetries.

Calculated critical-point energy (eV)	Band transition	Symmetry
7.77	$\Gamma_{15} \rightarrow \Gamma_1$	M_0
10.885	$L_3 \rightarrow L_2'$	M_0
10.893	$\Lambda_3 \rightarrow \Lambda_1$	M_1
12.35	$X_5' \rightarrow X_1$	M_0
13.04	$\Delta_5 \rightarrow \Delta_1$	M_1
13.3	$\Sigma_4 \rightarrow \Sigma_1$ $(4 \rightarrow 5)$	M_2
14.02	$X_5' \rightarrow X_3$	M_0
15.2	$L_3 \rightarrow L_3'$	M_0
15.35	$\Delta_1 \rightarrow \Delta_1$	M_1
15.43	$\Gamma_{15} \rightarrow \Gamma_{25}'$	M_0
15.57	$\Delta_5 \rightarrow \Delta_2$ $(3 \rightarrow 6)$	M_1
15.573	$\Sigma_4 \rightarrow \Sigma_1$ $(4 \rightarrow 6)$	M_1
15.576	$\Delta_5 \rightarrow \Delta_2$ $(4 \rightarrow 6)$	M_3
15.59	$L_1 \rightarrow L_2$	M_1
15.66	$\Sigma_3 \rightarrow \Sigma_1$	M_2
16.2	$\Lambda_3 \rightarrow \Lambda_3$	M_3
16.39	$\Sigma_4 \rightarrow \Sigma_2$	M_2
16.59	$\Sigma_1 \rightarrow \Sigma_1$ (forbidden)	M_2
16.63	$\Delta_5 \rightarrow \Delta_1$ $(4 \rightarrow 7)$	M_2
16.93	$X_4' \rightarrow X_3$	M_1
17.01	$\Delta_5 \rightarrow \Delta_1$ $(3 \rightarrow 7)$	M_3
18.3	$W(2 \rightarrow 5)$	M_3
18.4	$W(4 \rightarrow 6)$	M_3
18.99	$\Sigma_4 \rightarrow \Sigma_1$ $(4 \rightarrow 6)$	M_3
19.79	$W(4 \rightarrow 7)$, $(3 \rightarrow 6)$	M_3
19.92	$L_1 \rightarrow L_3'$	M_3
20.105	$K_1 \rightarrow K_1$	M_0
21.2	$W(3 \rightarrow 7)$	M_3
21.7	$\Sigma_1 \rightarrow \Sigma_1$ (forbidden)	M_3
21.704	$K_4 \rightarrow K_7$	M_3
24.755	$X(4 \rightarrow 7)$	M_3

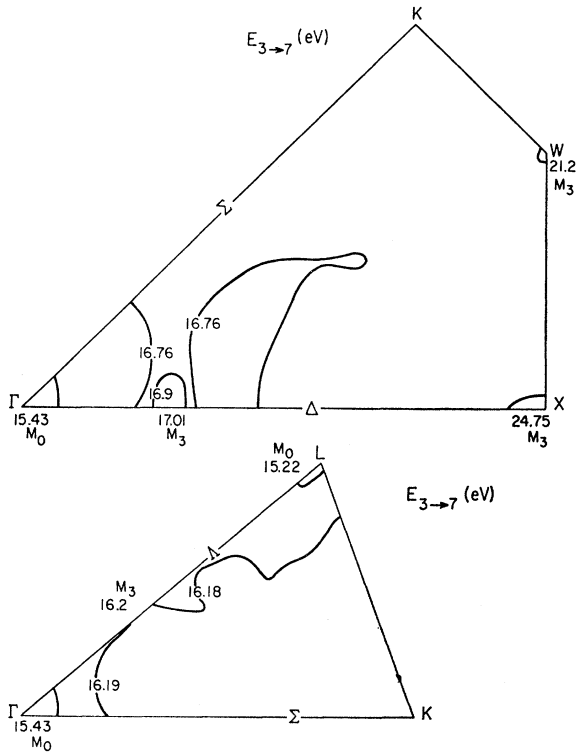

FIG. 14. Energy contours for $3 \rightarrow 7$ transitions in the ΓKL and ΓKWX planes.

we pick this as the plasma energy. The measured plasma energy quoted by RW is 22.2 eV.

Using the calculated values for $\epsilon_1(\omega)$ and $\epsilon_2(\omega)$ and the standard semi-infinite plane boundary conditions, the reflectivity $R(\omega)$ is calculated as a function of energy. This curve appears in Fig. 16. The peak in $\epsilon_1(\omega)$ below 8 eV causes a peak in $R(\omega)$ in this energy range; the next prominent structure is at 11 eV arising from $\Lambda_3 \rightarrow \Lambda_1$ transitions. The $R(\omega)$ curve strongly resembles the $\epsilon_2(\omega)$ in Fig. 3 for energies below 15 eV as is expected. The shapes, heights, and energies of the measured and calculated optical structure in this region are in good agreement. For higher energies, our reflectivity drops faster than the experiment. This is due to the fact that we have a low value of ϵ_2 for the L peak as previously discussed.

The functions $\epsilon_1(\omega)$ and $\epsilon_2(\omega)$ are also used to calculate $\mathrm{Im}[1/\epsilon(\omega)]$. This curve is plotted in Fig. 17. At low energies, the energies of the peaks in these curves exactly coincide while at high energies the shape is very close to the results of the electron-energy-loss experiment.

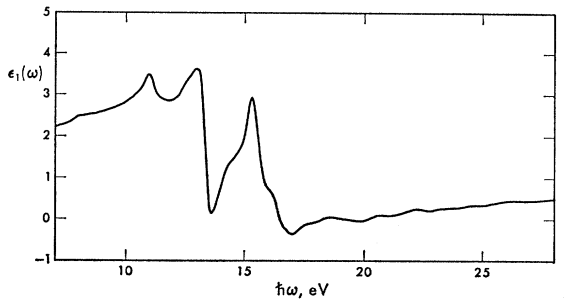

FIG. 15. The real part of the dielectric function as a function of energy.

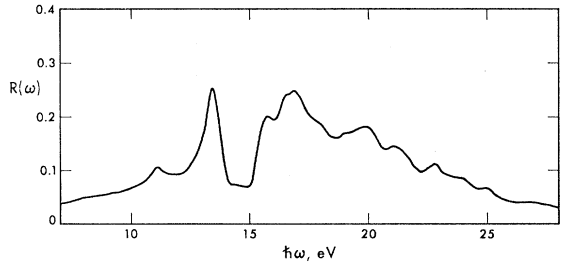

FIG. 16. The reflectivity as a function of energy.

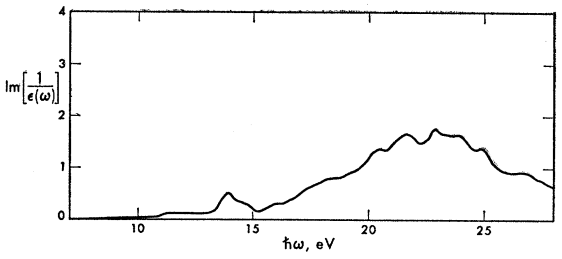

FIG. 17. The imaginary part of the reciprocal of the dielectric function as a function of energy.

DISCUSSION

In the previous section we have discussed the $\epsilon_2(\omega)$ spectrum in detail in terms of band transitions and cp's. In general, the agreement with experiment is very good over the entire range. In particular the energy positions and the shape of the main structure coincide quite well with the measured spectrum. The relative heights of the structure are also in agreement with experiment except for the Λ peak which is too low. Some possible explanations are: (1) the pseudo-wavefunctions are not giving accurate transition matrix elements, (2) excitonic structure, (3) local field corrections, or (4) the bands near Λ and L are not flat enough inside the zone and the potential should be altered. At present we do not know which of these possibilities is the most plausible, but calculations to investigate some of these are in progress. At high energies, the theoretical structure is shifted on the order of 1 eV from the measured spectrum. This is not a big difference since the potentials were adjusted to give the lower peaks accurately, and the range of interest is over 20 eV. Better agreement between theory and experiment can be obtained for high energies if an energy-dependent potential is used. Changes in the potential for high-energy electron states are expected since electrons in these states can probe the core and feel some of the strong core potential.

ACKNOWLEDGMENTS

We would like to thank Dr. D. M. Roessler and Professor W. C. Walker for sending us their data prior to publication and for helpful discussions. We would also like to thank John Walter for help with the computations.